Hydrol. Earth Syst. Sci. Discuss., 10, 13093–13144, 2013
www.hydrol-earth-syst-sci-discuss.net/10/13093/2013/
doi:10.5194/hessd-10-13093-2013

Hydrology and Earth System Sciences
Open Access
Discussions

Modeling glacier melt and runoff in a high-altitude headwater catchment in the Cordillera Real, Andes

T. Kinouchi[1], **T. Liu**[1], **J. Mendoza**[2], **and Y. Asaoka**[3]

[1]Department of Environmental Science and Technology, Tokyo Institute of Technology, Yokohama, Japan
[2]IHH, Universidad Mayor de San Andrés, Calle 30, Cota Cota, La Paz, Bolivia
[3]Department of Civil Engineering, Tohoku University, Sendai, Japan

Received: 19 September 2013 – Accepted: 21 October 2013 – Published: 4 November 2013

Correspondence to: T. Kinouchi (kinouchi.t.ab@m.titech.ac.jp)

Published by Copernicus Publications on behalf of the European Geosciences Union.

Abstract

Runoff from catchments with partial glacier cover is an integrated process of glacier melt, snowmelt, and surface and subsurface runoff of meltwater and rain from glacierized and non-glacierized areas. Additionally, inherent characteristics of the tropical Andes such as large meteorological variability, high elevation and steep slopes, hydrological effects of wetlands and lakes, and rapid glacier retreat make it difficult to model glacio-hydrological responses under changing climate. In this study, we developed a semi-distributed conceptual model applicable to partially glacierized catchments in the tropical Andes that considers all of these aspects, and we applied the model to the Huayna Potosi West headwater catchment in the Cordillera Real, Bolivia. Based on the latest 2 yr dataset of meteorological and hydrological monitoring, we showed the spatial and temporal variability of air temperature and precipitation in the region, and the dataset was used to calibrate model parameters and validate the performance of the daily runoff simulation. Variations in the simulated streamflow agreed well with the observed seasonal and temporal variations, and the result also showed that uncertainty pertaining to the spatial and temporal variations in air temperature and precipitation as well as the retarding effect of a wetland and lake strongly affected the runoff hydrograph. The simulated runoff components indicated that runoff from glacier melt occurs mainly in the initial period of the wet season, from October to early December, and in the late period of the wet season, March and April, although the runoff is relatively small in the latter period. Between these two periods in the wet season, major runoff components were estimated to be subsurface runoff in the non-glacierized area and surface runoff due to snowmelt. Given the future meteorological conditions based on the observational data and a predictive general circulation model output, the model quantified the long-term changes in runoff, glacierized area, and cumulative glacier and snow mass balance. The glacier retreat is estimated to continue to 2050, with the magnitude of area decrease and negative cumulative mass balance depending on the increasing temperature trend used. For higher temperature trends, in particular, greater

HESSD

10, 13093–13144, 2013

seasonal variation in runoff and larger contributions from subsurface runoff and surface runoff by rainfall were simulated to occur in the wet season, but the change in annual total runoff between the present and 2050 was not significant. These results suggest that it is important to consider how to best adapt to greater seasonal runoff variations in terms of water availability in the downstream region.

1 Introduction

It has been estimated that more than 99 % of tropical glaciers are located in the Andes: 71 % in Peru, 20 % in Bolivia, and 8 % in Ecuador, Colombia, and Venezuela (Kaser, 1999). However, these massive glaciers in the tropical Andes are retreating rapidly, as indicated by the decreasing area and length of selected glaciers (Vuille et al., 2008; Rabatel et al., 2013). The Cordillera Real, Bolivia, which contains 11 % of all the world's tropical glaciers and 55 % of the glaciers in Bolivia, lost more than 40 % of its glacier volume during the period of 1963 to 2006 (Soruco et al., 2009). A recent study revealed a continuous decrease in glacierized areas in the Cordillera Real, especially for relatively small glaciers (Liu et al., 2013). Future trends of individual glaciers are a serious public concern in the region because current water resources depend strongly on glacial meltwater (Vergara et al., 2007).

Tropical glaciers are thought to be an important indicator of global warming (Rabatel et al., 2003), and some glaciers in Bolivia have been monitored for more than two decades. Zongo Glacier has been the subject of numerous studies attempting to understand its mass balance, meteorological characteristics, and hydrological response (e.g. Soruco et al., 2009a). On the other hand, Chacaltaya Glacier (e.g. Ramirez and Francou, 2001; Francou et al., 2003) has already disappeared, and more glaciers are expected to follow (Rabatel et al., 2013). Even if the glaciers do not disappear completely, it can be expected that seasonal variation in streamflow will be enhanced and that less water will flow during the dry season because of decreased glacial meltwater

HESSD
10, 13093–13144, 2013

(Baraer et al., 2012). Furthermore, under growing population and the influence of climate change, it may become difficult to meet the water demands from various sectors.

In Bolivia, as in other countries in the Andes, water resources for drinking, agriculture, industry, and hydropower depend strongly on glacial meltwater. In urban centers in Bolivia such as La Paz and El Alto (population 2.3 million), glaciers of the Cordillera Real supply 30–40 % of potable water (Vergara et al., 2007). Tuni Lake, a reservoir located at the foot of the Cordillera Real, stores runoff from partially glacierized upstream catchments in which isolated glaciers such as Condoriri Glacier and Huayna Potosi West Glacier are located. Tuni Lake, along with Milluni Lake, supplies a major portion of the water used in the urban centers of La Paz and El Alto; it provides 86 % of the total supply to El Alto and 100 % of the supply to central La Paz. Milluni Lake also stores a portion of the meltwater from Zongo Glacier, which is located on the eastern side of the Huayna Potosi summit and has been studied extensively from meteorological and hydrological perspectives (e.g. Francou et al., 2003; Sicart et al., 2011).

Similar to the Zongo and Chacaltaya Glaciers, glaciers in the Tuni Lake catchment are also vulnerable to climate change. Therefore, assessing the impact of future climate change on glacier runoff and local water resources is an important and urgent issue for this region. We were able to locate advanced studies, such as trend and statistical analysis (Baraer et al., 2012), analysis based on global to regional climate model outputs (Vuille et al., 2008), and various applications of hydrological models for the Cordillera Blanca (e.g. Juen et al., 2007), but few studies regarding predictive hydrological models and their application to partially glacierized catchments in the Cordillera Real are available (Moya et al., 2013).

For partially glacierized catchments, runoff from non-glacierized areas is an essential component in addition to glacier melt and the resulting runoff from glacierized areas. The application of a predictive runoff model to partially glacierized catchments in the tropical Andes is limited to studies by Pouyaud et al. (2005), Juen et al. (2007), and Baraer et al. (2012) for the Cordillera Blanca and to Ribstein et al. (1995) and Ca-

HESSD
10, 13093–13144, 2013

ballero et al. (2004) for the Cordillera Real. These models simulated annual (Pouyaud et al., 2005; Baraer et al., 2012), seasonal (Ribstein et al., 1995; Juen et al., 2007), or daily (Caballero et al., 2004) streamflows. In other regions, such as the Alps and North America, a similar hydrological modeling approach has been used (e.g. Moore, 1993; Schaper et al.,1999; Schaefli et al., 2005; Stahl et al., 2008) by focusing on the relevant processes in each study area. Snowmelt Runoff Models (SRM) (Martinec et al., 2008) are used widely to compute daily runoff considering snow and glacier hydrology (Nolin et al., 2010). The application of distributed hydrological models to glacierized catchments has the advantage of accounting for the spatial distribution of precipitation, air temperature, and other dominant factors, as well as glacier melt and snow accumulation. Such an approach has been applied to partially glacierized catchments in Himalaya (Konz et al., 2007), Alps (Huss et al., 2008) and Canadian Rocky (Naz et al., 2013). In general, distributed models tend to require large amounts of weather data from multiple stations to represent the spatial distribution of meteorological forcing and glacier thickness and area, but these data may be difficult to obtain in remote high-mountain catchments.

Striving for practical use in water resources management while maintaining scientific robustness, our study had the goal of developing a semi-distributed conceptual model that could simulate runoff in a partially glacierized high-mountain catchment in the tropical Andes. The model was designed to calculate runoff on a daily basis considering the inherent characteristics of catchments in the tropical Andes, i.e. high-altitude steep-slope topographic conditions, spatially and temporally variable meteorological conditions, hydrological effects of wetlands and lakes, and changes in glacierized areas related to glacier mass balance (for long-term prediction), by fully utilizing geographical information and meteorological and hydrological data obtained in the study area since 2011. We applied the model to a partially glacierized headwater catchment in the Cordillera Real and quantified current seasonal streamflow variations and the components contributed from different sources of runoff. We also investigated how local variability in meteorological conditions affects the runoff. Finally, long-term hydrolog-

HESSD
10, 13093–13144, 2013

ical impacts of climatic changes were quantified considering glacier retreat and the resulting changes in glacierized areas to the year 2050.

2 Study area

The Huayna Potosi West headwater catchment (Fig. 1; 7.99 km^2) was selected to demonstrate the applicability of the semi-distributed conceptual model developed in this study. The elevation of the catchment ranges from about 4800 m to 6088 m a.s.l., and its upstream region includes the Huayna Potosi Glacier area (16°16′ S, 68°9′ W). The land surface of the catchment is covered mostly by unvegetated soil and gravel, and glaciers occupied 18.2 % of the total catchment area in 2010. Figure 1 shows the distribution of glacierized areas obtained from Landsat TM images with the band ratio method verified by Liu et al. (2013). About 52 % of the glacier surface is below 5200 m a.s.l.; fragmented smaller glaciers exist above this elevation. The east side of the Hyana Potosi Glacier has been studied by the French Research Institute for Development (IRD) since 1991 (Francou et al., 1995; Ribstein et al., 1995). In the study area, a shallow lake with a surface area of about 0.044 km^2 has developed in the middle of the stream. A wetland located downstream of the lake covers a larger area (0.248 km^2) and is at times filled by outflow from the upstream region. Therefore, both the wetland and the lake likely play a role in retarding the runoff from the glacierized and non-glacierized areas. Streamflow from the headwater catchment, after merging with other streams, is partly diverted to Tuni Lake.

3 Characteristics of meteorological and hydrological conditions

Meteorological and hydrological variables are measured at automatic whether stations (AWSs) within and outside the catchment (Fig. 1). The water level of the stream is monitored by a pressure-transducer gage located at the downstream outlet (HH1), and these data are converted to time series of flow rate using a rating curve confirmed

HESSD
10, 13093–13144, 2013

by field measurements. Meteorological variables such as air temperature, relative humidity, wind velocity, shortwave radiation, air pressure, and precipitation are monitored at three AWSs, which are located on the glacier surface at MHG (5150 m a.s.l.) and in non-glacierized areas at MH1 (4736 m a.s.l.) and MT1 (4472 m a.s.l.) at distances of 0.6 and 8.0 km from HH1, respectively. Incident and reflected longwave and shortwave radiation are measured at MHG. Additionally, two pluviometers located at PT1H (4736 m a.s.l.) and PT2H (4915 m a.s.l.) provide data of monthly precipitation with high catch efficiency for calibrating the daily precipitation measured at MH1 and MHG. Considering the period of available data and the flow patterns, we conventionally defined the hydrological year (HY) as starting in June and ending in May of the next year.

Figure 2 shows daily mean air temperature obtained at three AWSs and relative humidity, solar radiation, precipitation, and flow rate measured at MH1. The 2 yr dataset clearly indicates two distinct seasons, dry and wet, reflected in the relative humidity, precipitation, and flow rate. A good correlation for air temperature was found between MH1 and MHG (R^2 = 0.77) during the 2 yr, implying that similar variation may have occurred in the ablation zone. At both MH1 and MHG, relatively high air temperatures are observed in the early wet season from October to early December as well as at some times during the late wet season in March. From December to February, air temperatures are relatively low but still higher than those in the dry season, May to August. Similarly, solar radiation is highest in the early wet season, but this is followed by relatively low and more fluctuating solar radiation that depends on the cloudiness and precipitation. Streamflow is relatively large and variable in the wet season but much smaller in the dry season. The magnitude and variation of streamflow are affected by precipitation, snowmelt, glacier melt, and evaporation, which are related to air temperature, humidity, solar radiation, and other radiative fluxes. In the hydrological year of 2011 (beginning in June 2011; hereafter HY2011), three individual peaks corresponding to higher temperature, higher solar radiation, and lower humidity occurred in the period between October and December, and each peak was followed by an abrupt decrease within a short period of time. From the dataset, we found that air tempera-

HESSD
10, 13093–13144, 2013

ture was more strongly correlated with flow rate during this period, with a phase lag of about 5 days, which suggests that a retarding effect exists in this catchment, probably because of the small lake and wetland in the catchment. In HY2012, fewer clear individual peaks occurred. In this case, the contribution of glacier melt to streamflow is unclear because streamflow peaks can form by snow and/or glacier melting or by direct runoff of rainfall.

The lapse rate of the air temperature is an important index for defining the air temperature spatial distribution, especially in the ablation zone. In hydrological modeling of catchments covered by snow and glacier, the lapse rate is typically given as a constant throughout a certain period, i.e. a year or month. However, our data indicated significant variations in the lapse rate between both MH1 – MHG and MT1 – MH1 (Fig. 3). When the air was relatively dry, which is typical for the dry season, the lapse rate between MH1 and MHG became close to the dry adiabatic lapse rate (= 1.0), but in the wet season, it tended to be closer to that between MT1 and MH1 (dotted line in Fig. 3). The vertical gradient of precipitation was observed from both the pluviometers and rain gages, which indicated strong height dependency in the wet season, with exceptions in some months (Fig. 4). Although these data were obtained from a limited number of stations, both air temperature and precipitation are highly variable in time and space over the study area. Therefore, it is important to understand the influences of the temporal and spatial variability of the meteorological conditions on the catchment-scale hydrological response through melting, accumulation, and runoff.

Compared with the Cordillera Blanca, Peru, where more studies related to glacier melt and hydrological response have been conducted (e.g. Mark and Seltzer, 2005; Juen et al., 2007), our study field exhibits different seasonal variations and magnitudes of meteorological and hydrological variables. In the Cordillera Real, including Zongo Glacier (Ribstein et al., 1995), a shorter wet season and lower annual precipitation occur. The seasonal variation in air temperature is not very different, but higher temperature is observed in the Cordillera Real compared with that measured in a similar elevation zone in the Cordillera Blanca (Mark and Seltzer, 2005). These conditions in

HESSD
10, 13093–13144, 2013

the Cordillera Real all tend to enhance glacier and snow melting during accumulation periods, which may result in a larger seasonal variation in runoff and a more sensitive response to climate variability in the future compared with the Cordillera Blanca.

4 Glacier melt and runoff modeling

To estimate streamflow in highland catchments of the tropical Andes under changing climate, we followed the approach, employed in many previous studies for glacierized catchments (e.g. Martinec et al., 2008), of dividing the catchment into multiple elevation zones and linearly combining the runoff from glacierized and non-glacierized areas in each zone to obtain the total discharge of the entire catchment. Our model considers spatial and temporal variability in meteorological conditions by taking advantage of monitoring data obtained at multiple locations in the study area during 2011 and 2013.

In the runoff modeling, we attempted to include a variety of processes related to the watershed-scale hydrological cycle. The structure of the runoff calculation in glacierized and in non-glacierized areas for each elevation zone is shown schematically in Fig. 5. The runoff components considered in the model are surface flow, subsurface flow, and deep groundwater flow, but we consider that deep groundwater does not contribute to streamflow in the headwater catchment. Either snow or rain is assumed to fall on glacier ice or on a snow surface over the glacierized area, whereas these fall onto ground or onto snow surface over the non-glacierized area. Sublimation from snow and glacier ice and evaporation from the ground surface were calculated. The subsurface and deep groundwater flows were modeled conceptually by relating them to a single storage reservoir in each elevation zone. The retarding effect of the wetland and lake was considered in the model, although this is not included in Fig. 5.

Runoff from non-glacierized areas in each elevation zone i, $q_{ng,i}$, is formulated by Eq. (1) through Eq. (7), which compute the total surface runoff from rain and snowmelt and the base flow from the storage reservoir. Snowmelt is estimated by Eq. (4), in which both air temperature and solar radiation are additive factors (Hock, 2003).

HESSD
10, 13093–13144, 2013

$$q_{ng,i} = q_{ngs,i} + q_{ngr,i} + q_{ngb,i} \quad (1)$$

$$q_{ngs,i} = c_{ngs} M_{ngs,i} \quad (2)$$

$$q_{ngr,i} = P_{ngr,i} - \min((1 - c_{ngr}) P_{ngr,i}, \mathrm{Inf}) \quad (3)$$

$$M_{ngs,i} = a_{1s} T_{ng,i} + a_{2s}(1 - \alpha_{s,i})\mathrm{SR}_i \cdot S\downarrow \quad (4)$$

$$\alpha_{s,i} = \alpha_{snow,i} + \left(\alpha_{gnd} - \alpha_{snow,i}\right)\left(1 + s_{ngw,i}/s^*\right)^{-3} \quad (5)$$

$$\alpha_{snow,i} = \alpha_{firn} + (\alpha_{fresh} - \alpha_{firn}) \exp\left(-n_i/n^*\right) \quad (6)$$

$$q_{ngb,i} = k_{ng} S_{ng,i}. \quad (7)$$

In the equations above, $q_{ngs,i}$ and $q_{ngr,i}$ are the surface runoff from snowmelt and rainfall ($\mathrm{mm\,d^{-1}}$), respectively, $q_{ngb,i}$ is the subsurface flow ($\mathrm{mm\,d^{-1}}$) generated from storage in the ground $S_{ng,i}$ (mm), $P_{ngr,i}$ is the daily rainfall on the non-glacierized area ($\mathrm{mm\,d^{-1}}$), $M_{ngs,i}$ is the daily snowmelt on the non-glacierized area ($\mathrm{mm\,d^{-1}}$), a_{1s} and a_{2s} are melting factors, $T_{ng,i}$ is the air temperature (°C), $S\downarrow$ is the daily mean downward shortwave radiation ($\mathrm{Wm^{-2}}$), c_{ngr} and c_{ngs} are the runoff coefficients for rainfall and snowmelt over the non-glacierized area, respectively, SR_i is a topographic shading factor to account for the effect of reduced solar radiation caused by shading from surrounding slopes, and k_{ng} is a constant ($\mathrm{day^{-1}}$). Surface albedo, $\alpha_{s,i}$, is calculated using Eqs. (5) and (6) (Sicart et al., 2011), where $\alpha_{snow,i}$, α_{gnd}, α_{firn}, and α_{fresh} are the albedo of snow surface (variable), ground surface, firn, and fresh snow, respectively, $s_{ngw,i}$ is the snow water equivalent in the non-glacierized area (mm), n is the number of days since the last snowfall, and s^* and n^* are constants. The albedo of fresh snow was set to depend on air temperature. Storage in the ground is calculated from the water balance equation (Eq. 8):

$$\frac{\mathrm{d}S_{ng,i}}{\mathrm{d}t} = P_{ngr,i} - q_{ngr,i} + f_i - E_{ng,i} - q_{ngb,i} \quad (8)$$

HESSD
10, 13093–13144, 2013

$$f_i = \begin{cases} \min(M_{\mathrm{ng},i}, \mathrm{Inf}) & \text{if } s_{\mathrm{ngw},i} > 0 \\ 0 & \text{if } s_{\mathrm{ngw},i} = 0 \end{cases} \quad (9)$$

$$M_{\mathrm{ng},i} = (1 - c_{\mathrm{ngs}}) M_{\mathrm{ngs},i} \quad (10)$$

$$\frac{\mathrm{d}s_{\mathrm{ngw},i}}{\mathrm{d}t} = P_{\mathrm{ngs},i} - M_{\mathrm{ngs},i} - E_{\mathrm{ngs},i}, \quad (11)$$

where f_i is infiltration into the ground due to snowmelt ($\mathrm{mm\,d^{-1}}$), $E_{\mathrm{ng},i}$ is evaporation from the ground surface ($\mathrm{mm\,d^{-1}}$), $M_{\mathrm{ng},i}$ is snowmelt that can contribute to infiltration ($\mathrm{mm\,d^{-1}}$), Inf is the maximum capacity of infiltration ($\mathrm{mm\,d^{-1}}$), $P_{\mathrm{ngs},i}$ is snowfall ($\mathrm{mm\,d^{-1}}$), and $E_{\mathrm{ngs},i}$ is sublimation from the snow surface ($\mathrm{mm\,d^{-1}}$).

Runoff from the glacierized area in each elevation zone i, $q_{\mathrm{g},i}$, is computed as the total of surface runoff from glacier melt and snowmelt as well as direct runoff from rainfall. Wagnon et al. (1998) reported that subglacial flow, depending on the season, plays a role in generating a slow runoff component, but we assumed in our model simulations that neither subsurface flow nor recharge into the ground occurs beneath the glacier, although the model can calculate this processes. Glacier melt and snowmelt were formulated by the multiplicative temperature-index model (Hock, 1999; Pellicciotti et al., 2005; Huss et al., 2008), in which the integrated melting factor varies depending on the incident solar radiation, the albedo of the glacier or snow surface, and the topographic shading (Eqs. 16 and 17). Glacier melt was assumed to occur when no snow accumulation exists on the glacier ice. If rainfall occurs, we assumed that a portion of the rainfall becomes surface runoff irrespective of the existence of snow over the glacier and that the rest accumulates as solid water on the glacier surface. These concepts are formulated by Eq. (12) through (18). Eq. (18) is used in conjunction with Eq. (6).

$$q_{\mathrm{g},i} = q_{\mathrm{gm},i} + q_{\mathrm{gs},i} + q_{\mathrm{gr},i} \quad (12)$$

HESSD
10, 13093–13144, 2013

$$q_{\mathrm{gm},i} = c_{\mathrm{gm}} M_{\mathrm{g},i} \quad \text{if } s_{\mathrm{gw},i} = 0 \tag{13}$$

$$q_{\mathrm{gs},i} = c_{\mathrm{gs}} M_{\mathrm{gs},i} \quad \text{if } s_{\mathrm{gw},i} > 0 \tag{14}$$

$$q_{\mathrm{gr},i} = c_{\mathrm{gr}} P_{\mathrm{gr},i} \tag{15}$$

$$M_{\mathrm{g},i} = (a_{1\mathrm{g}} + a_{2\mathrm{g}}(1 - \alpha_{\mathrm{gs},i}) SR_i \cdot S\downarrow) \cdot T_{\mathrm{g},i} \quad (s_{\mathrm{gw},i} = 0) \tag{16}$$

$$M_{\mathrm{gs},i} = (a_{1\mathrm{gs}} + a_{2\mathrm{gs}}(1 - \alpha_{\mathrm{gs},i}) SR_i \cdot S\downarrow) \cdot T_{\mathrm{g},i} \quad (s_{\mathrm{gw},i} > 0) \tag{17}$$

$$\alpha_{\mathrm{gs},i} = \alpha_{\mathrm{snow},i} + \left(\alpha_{\mathrm{ice}} - \alpha_{\mathrm{snow},i}\right) \left(1 + s_{\mathrm{gw},i}/s^*\right)^{-3}. \tag{18}$$

In the equations above, $q_{\mathrm{gm},i}$ is the surface runoff due to glacier melt (mm d^{-1}), $q_{\mathrm{gs},i}$ and $q_{\mathrm{gr},i}$ are the surface runoffs due to snowmelt and rainfall on the glacier surface (mm d^{-1}), respectively, $M_{\mathrm{g},i}$ and $M_{\mathrm{gs},i}$ are melt of the glacier and melt of snow on the glacier (mm d^{-1}), respectively, $P_{\mathrm{gr},i}$ is the daily rainfall on the glacierized area (mm d^{-1}), $T_{\mathrm{g},i}$ is the air temperature on the glacier surface (°C), $s_{\mathrm{gw},i}$ is the snow water equivalent (mm), c_{gm}, c_{gs}, and c_{gr} are the runoff coefficients of glacier melt, snowmelt, and rainfall, respectively, $a_{1\mathrm{g}}$ and $a_{2\mathrm{g}}$ are melting factors for glacier ice, $a_{1\mathrm{gs}}$ and $a_{2\mathrm{gs}}$ are melting factors for snow on the glacier ice, $\alpha_{\mathrm{gs},i}$ is the surface albedo in the glacierized area, and α_{ice} is the albedo of glacier ice. The snow water equivalent $s_{\mathrm{gw},i}$ on the glacier surface is calculated by the water balance as

$$\frac{ds_{\mathrm{gw},i}}{dt} = P_{\mathrm{gs},i} + (1 - c_{\mathrm{gr}}) P_{\mathrm{gr},i} - q_{\mathrm{gs},i} - E_{\mathrm{gs},i}, \tag{19}$$

where $P_{\mathrm{gs},i}$ is snowfall (mm d^{-1}), and $E_{\mathrm{gs},i}$ is sublimation of snow (mm d^{-1}).

The total runoff, Q (m^3 s^{-1}), is calculated as the sum of the individual runoff components in each elevation zone:

$$Q = \alpha \left(\sum_i A_{\mathrm{ng},i} q_{\mathrm{ng},i} + \sum_i A_{\mathrm{g},i} q_{\mathrm{g},i} \right), \tag{20}$$

HESSD
10, 13093–13144, 2013

where $A_{ng,i}$ and $A_{g,i}$ are the non-glacierized and glacierized areas in each elevation zone (km^2), respectively, and α is the unit conversion factor (= 1000/24/3600).

Sublimation from the snow surface is computed by Eq. (21) (Wanchang et al., 1999). Evaporation from the ground surface, $E_{ng,i}$, is assumed to be equal to potential evaporation if sufficient water exists in the ground; otherwise, it is set equal to the storage in the ground S. Potential evaporation from the ground is computed by the Priestley–Taylor method (Eq. 24). According to our monitoring data, precipitation is mostly limited to a certain period of time. Thus, we applied these equations even on days with precipitation.

$$E_{ngs,i} \text{ or } E_{gs,i} = 0.24u_1(e_{sa,i} - e_{a1,i}) \quad (21)$$

$$e_{sa,i} = 6.11 \times 10^{7.5T_{ng,i}/(237.3+T_{ng,i})} \quad (22)$$

$$E_{ng,i} = \begin{cases} \mathrm{POT}_{ng,i} \ (S_{ng,i} > \mathrm{POT}_{ng,i}) \\ S_{ng,i} \ (S_{ng,i} < \mathrm{POT}_{ng,i}) \end{cases} \quad (23)$$

$$\mathrm{POT}_{ng,i} = \alpha_{PT} \cdot \frac{\Delta}{\lambda \cdot (\Delta + \gamma_p)} \cdot R_{n,i} \quad (24)$$

$$\Delta = \frac{de_{sa,i}}{\mathrm{d}T} \quad (25)$$

$$\gamma_p = \frac{c_p p}{0.622\lambda}. \quad (26)$$

In the equations above, $\mathrm{POT}_{ng,i}$ is the potential evapotranspiration (mm d^{-1}), u_1 and $e_{a1,i}$ are the wind velocity (m s^{-1}) and vapor pressure (hPa) 1 m above the ground, respectively, $e_{sa,i}$ is the saturation vapor pressure (hPa), α_{PT} is an empirical constant (= 1.26), γ_p is a psychrometric constant, p is the atmospheric pressure (hPa), c_p is the specific heat at constant pressure (J kg^{-1} K^{-1}), λ is the latent heat of vaporization (= $2.5 \times 10^6 - 2370T_{ng,i}$ J kg^{-1}), $R_{n,i}$ is the net radiation (W m^{-2}), and Δ is the rate of change of the saturation vapor pressure with respect to air temperature.

HESSD
10, 13093–13144, 2013

The air temperature over the non-glacierized and glacierized areas is given by Eqs. (27) and (28), respectively, using the daily or monthly lapse rate calculated from the air temperature monitored at three locations, i.e. MT1, MH1, and MHG. We assumed the lapse rate over the glacierized areas to be the average of those obtained from MT1 – MH1 and MH1 – MHG (Eq. 29). Over the non-glacierized area, the lapse rate obtained from MT1 – MH1 was used. Even though the ablation zone lies in lower elevations, between 5000 and 5200 m a.s.l., interpolation of the air temperature at the ablation zone from these stations may include uncertainty due to a local warming or cooling effect.

$$T_{\mathrm{ng},i} = T_{\mathrm{MH1}} + \gamma_{\mathrm{L1}}(z_i - z_{\mathrm{MH1}}) \tag{27}$$

$$T_{\mathrm{g},i} = T_{\mathrm{MH1}} + \gamma_L(z_i - z_{\mathrm{MH1}}) \tag{28}$$

$$r_L = \begin{cases} \gamma_{L1}\ (z_i < z_{\mathrm{MH1}}) \\ (\gamma_{L1} + \gamma_{L2})/2\ (z_{\mathrm{MHG}} > z_i > z_{\mathrm{MH1}}) \\ \gamma_{L2}\ (z_i > z_{\mathrm{MHG}}) \end{cases}. \tag{29}$$

In the above, T_{MH1} is the observed air temperature at MH1 (°C), z_i, z_{MH1}, and z_{MHG} are the elevation at elevation zones i, MH1, and MHG (m), respectively, and γ_{L1} and γ_{L2} are the observed lapse rates between MT1 and MH1 and between MH1 and MHG, respectively. The daily precipitation at each elevation zone for non-glacierized ($P_{\mathrm{ng},i}$) and glacierized ($P_{\mathrm{g},i}$) areas is calculated from

$$P_{\mathrm{ng},i} = P_{\mathrm{g},i} = P_{\mathrm{MH1}}\left[1 + \gamma(z_i - z_{\mathrm{MH1}})/100\right], \tag{30}$$

where P_{MH1} is the daily precipitation measured at MH1 (mm d^{-1}), γ is the vertical gradient of precipitation per 100 m of altitude difference given by $\gamma = 100\Delta P/(P\Delta z)$, where ΔP is the difference between the observed monthly precipitation at PT1H and PT2H, Δz is the altitude difference between PT1H and PT2H, and P is the monthly precipitation at MH1 (= PT1H). The precipitation phase is determined based on the temperature

HESSD
10, 13093–13144, 2013

threshold, i.e. 2 (°C) in this model, below which all precipitation falls as snow ($P_{ngs,i}$ and $P_{gs,i}$). Otherwise, it falls as rain ($P_{ngr,i}$ and $P_{gr,i}$).

The glacier lake and wetland act as a retarding basin by temporally storing runoff from the glacierized and non-glacierized areas. The combined effect of the lake and wetland is formulated by Eqs. (31) and (32):

$$A\frac{dh}{dt} = Q_{in} - Q_{out} \quad (31)$$

$$Q_{out} = CL(h - h_L)^{3/2}, \quad (32)$$

where A and h are the total surface area (m^{-2}) and water surface elevation of the retarding basin (m a.s.l.), respectively, Q_{in} is the inflow to the retarding basin ($m^3 s^{-1}$), which is equal to Q given by Eq. (20), Q_{out} is the outflow from the retarding basin ($m^3 s^{-1}$), h_L and L are the bottom elevation (m a.s.l.) and width of the outlet from the retarding basin (m), respectively, and C is the hydraulic constant.

A glacier retreats or advances based on mass balance and glacier dynamics. In our study area, glacier velocity is very small compared to that of Zongo (20 m a^{-1} between 4900 and 5200 m a.s.l.) (Soruco et al., 2009) because the size of the glacier is also small. Therefore, we do not consider glacier advance, and assume that area change occurs only by retreat.

The glacierized area decreases depending on the volume of melted and sublimated glacier ice. This process is incorporated into the model using a volume–area relationship:

$$V = C_s A_g^{\beta}, \quad (33)$$

where V is the volume of glacier ice (km^3), A_g is the total area of glacier surface (km^2), and C_s and β are scaling parameters. As the change in glacier volume resulting from melting and sublimation is calculated, the change in total glacierized area ΔA_g (km^2) is obtained by Eq. (34), which is derived from Eq. (33):

HESSD
10, 13093–13144, 2013

$$\Delta A_g = \frac{\Delta V}{C_s \beta A_g^{\beta-1}}, \quad (34)$$

where ΔV is the change in the total volume of glacier ice during each day (km^3), which is calculated from the daily amount of melting and sublimation summed over each elevation zone. Sublimation of glacier ice is estimated after Ohno et al. (1992). Once the change in total glacierized area is calculated, it is prorated to each elevation zone by the ratio of the volume change in each elevation zone, ΔV_i, to that of the total volume, ΔV, which is expressed by

$$\Delta A_{g,i} = A_{g,i}^{t+1} - A_{g,i}^{t} = \frac{\Delta V_i}{\Delta V} \Delta A_g, \quad (35)$$

where $\Delta A_{g,i}$ is the daily change of glacierized area in each elevation zone i between time steps t and $t+1$.

5 Input data and parameter settings

The Huayna Potosi West headwater catchment was divided into 100 m elevation zones using ASTER 30 m Global DEM data. Glacierized areas were calculated for each elevation band from a glacier boundary map delineated from a LANDSAT TM image taken in 2010 by applying the method verified by Liu et al. (2013). The areas of the lake and wetland were manually obtained from the same satellite image.

Glacier melt and snowmelt were formulated to depend on the air temperature and solar radiation, as explained earlier. The air temperature for each elevation zone is given by Eqs. (31)–(33). For solar radiation, data measured at MH1 were used. For precipitation, rain gauge data at MH1 and MHG were used to provide daily precipitation after calibration with the monthly totals measured at PT1H and PT2H. The vertical gradient of precipitation is set according to the monthly precipitation at stations PT1H and PT2H

HESSD
10, 13093–13144, 2013

and applied to all elevation zones. The differences in annual mean relative humidity and wind velocity between MH1 and MHG are 5.6 % and 0.04 m s^{-1}, respectively, thus we used relative humidity and wind velocity measured at MH1 as representative conditions for the entire catchment.

In the equations of snowmelt and glacier melt, two melting factors need to be calibrated. For snowmelt, the melting factors are manually calibrated to have a closer match between the measured and calculated albedo on the glacier surface at MHG (5150 m a.s.l), whereas for glacier melting these factors are manually calibrated to reproduce three individual peaks observed at HH1 in 2011. Then, the melting factors are determined to be constant throughout the year (Table 1). The root mean square error of simulated and observed flow rates are minimized through these calibration processes. The calibrated melting factors are further validated by comparing observed annual glacier mass balance in each elevation zone in Zongo Glacier, which is located in the same region, with those calculated by Eqs. (16) and (17). The results confirmed that these melting factors are suitable for simulating the glacier and snow melts in our study area. For scaling parameters C_s and β in Eq. (33), two settings are used to consider the uncertainty relating to the glacier volume–area relationship. In one setting (case A), C_s and β are set to 0.04088 and 1.375, respectively, based on a regression analysis of isolated glaciers located in the tropical Andes in Bolivia and Peru (Baraer et al., 2012). In another setting (case B), C_s and β are set to 0.03530 and 1.375, respectively, to consider two main separated glaciers in our study area by a single volume–area relationship (Baraer et al., 2012). The setting of case A is used to simulate current and future seasonal streamflow variations, while both settings (cases A and B) are applied for understanding uncertainty in long-term changes in glacierized area and cumulative mass balance.

The topographic shading factor is obtained for each elevation band based on the Aster 30 m global DEM using Solar Analyst (Fu and Rich, 2000). Parameters used for calculating albedo change are after Sicart et al. (2011) and were adjusted to provide better agreement during the entire periods (Table 2). The constant for subsurface out-

HESSD
10, 13093–13144, 2013

flow from storage, k_{ng}, is determined from the tailing curve of the observed hydrograph. Maximum storage capacity (S_{max}) and infiltration rate (Inf) of the ground are set based on data from the sampled soil cores. In glacierized areas, runoff coefficients for rainfall (c_{gr}), snowmelt (c_{gs}) and glacier melt (c_{gm}) were determined to be unity. Runoff coefficients for the snowmelt (c_{ngs}) and rainfall (c_{ngr}) in the non-glacierized area were formulated to depend on the storage of the underlying soil layer in each elevation zone, i.e.

$$c_{ngs} = c_{ngr} = c_{ngs,min} + (c_{ngs,max} - c_{ngs,min}) \frac{S_{ng,i}}{S_{max}}, \quad (36)$$

where $c_{ngs,min}$ and $c_{ngs,max}$ are the lower and upper bound of the runoff coefficient, respectively, which values are manually calibrated to give a closer match of simulated flow rates with those observed in the wet season (Table 2).

6 Simulation conditions for future prediction

Meteorological forcing such as air temperature and precipitation needs to be provided for prediction of future runoff. In this study, we simply calculated future glacier melt and runoff based on current meteorological conditions and future trends found from observational data. A similar approach was used by Stahl et al. (2008) to predict the impact of future climate change on water resources from glacial meltwater, but few studies are available for catchments in the tropical Andes.

General circulation model (GCM) outputs are also used for prediction of future runoff in glacierized catchments (Stahl et al., 2008). For catchments with a size far less than that of the grid resolved by the GCM, physical or statistical downscaling methods are sometimes employed to evaluate spatial distribution within the grid size of the GCM. However, downscaling remains challenging, especially for high mountain regions with limited data such as the Cordillera Real. Therefore, we attempted to use one GCM output (MRI-AGCM), simulated by the Meteorological Research Institute, Japan, (MRI)

HESSD
10, 13093–13144, 2013

with a high-resolution (20 km) grid system and without the introduction of a downscaling technique.

Observed trends in air temperature in the tropical Andes have been reported by several researchers focusing on vertical structure. Vuille and Bradley (2000) indicated, based on 268 station records from 0 to 5000 m elevation during 1939–1998, that the trend of near-surface temperature ranges from 0.11 °C decade^{-1} to 0.34 °C decade^{-1} depending on the period, with the larger trend in the recent period. Additionally, they showed a decrease in the warming trend with elevation, but the vertical difference in the trends was not notable. Mark and Seltzer (2005) analyzed temperature records from 29 stations in the Cordillera Blanca that showed an average increasing trend of 0.26 °C decade^{-1} over the 37 yr interval from 1962 to 1999 and an increasing trend of 0.39 °C decade^{-1} when the period from 1951 to 1999 was considered. Pepin and Lindquist (2008) analyzed temperature trends at 1084 stations worldwide ranging in elevation from 500 m to 4700 m and reported a weak decrease in trend magnitude with elevation in the Tropics, although great scatter existed in plots. On the other hand, predicted air temperature distributions indicate that air temperature at higher elevation will be more strongly influenced by climate change in future periods (Bradley et al., 2006). According to their result of air temperature increase from 1990–1999 to 2090–2099 calculated from the outputs of eight different GCMs employed in the 4th Assessment of the Intergovernmental Panel on Climate Change (IPCC) using the SRES A2 scenario, we can find the temperature trend in the region on which we focus (about 16° S) to be more than 0.45 °C decade^{-1}.

To understand historical trends in precipitation, Vuille et al. (2003) used records from 42 stations in the tropical Andes between 1950 and 1994 and indicated that precipitation decreased at most stations in southern Peru and along the Peru/Bolivia border. However, the trend was not significant for annual and seasonal precipitation for stations above 2500 m a.s.l. Rabatel et al. (2013) concluded that precipitation has not displayed a significant, spatially coherent trend in the tropical Andes since the middle of the 20th century. Vuille et al. (2003) also indicated that relative humidity showed a moderate

HESSD
10, 13093–13144, 2013

increasing trend (0.5–1.0 % decade^{-1}) for southern Peru, western Bolivia, and northernmost Chile from 1950 to 1994, but trends from 1979 to 1995 were not significant, and values were much lower or even negative.

Most of the models used for the IPCC-AR4 report predict an increase in precipitation in the tropical Andes during the wet season and a decrease during the dry season (Vera et al., 2006; Vuille et al., 2008). Urrutia and Vuille (2009) indicated, using a regional climate model (PRECIS) with the A2 scenario, that precipitation will decrease in the future along the western slopes of the tropical Andes above 4000 m a.s.l. but that no significant difference will occur along the eastern slope. Kitoh et al. (2011) predicted with a high-resolution GCM that in the Bolivian Andes precipitation will increase in the wet season toward the end of the 21st century. According to their results for the near future, to 2039, the rates of increase in annual precipitation and mean air temperature are calculated to be 6.4 mm and 0.040 °C per year, respectively.

Based on this review of past and future trends in air temperature and precipitation, we applied the model to predict streamflow and change in glacierized area under the following two cases of future meteorological scenarios: (1) the current observed conditions of air temperature increases gradually into the future with specified long-term trends, and (2) the predicted climate change occurs under a specific CO_2 emission scenario (SRES A1B scenario), for which MRI-AGCM outputs were used (Kitoh et al., 2011).

For the first case, we assumed several constant trends of near-surface temperature ranging from 0 to 0.4 °C decade^{-1} over the entire catchment, which means that air temperature will increase uniformly in the vertical and horizontal domains. We also applied the same lapse rate obtained from our current meteorological data. For precipitation, we assumed that no trend exists and that the observed daily precipitation is preserved into the future with the same magnitude and temporal and spatial patterns. This assumption is based on findings from an analysis of observed precipitation (Vuille et al., 2008) and the comprehensive review by Rabatel et al. (2013), in which the authors concluded that precipitation has not displayed a significant, spatially coherent trend in

HESSD
10, 13093–13144, 2013

the tropical Andes since the middle of the 20th century. Vertical gradients were from monthly precipitation observed at two sites, PT1H and PT2H, and we assumed that the same gradient applies to the highest elevation zone. For the second case, we used MRI-AGCM outputs of the near-future period (2015 to 2039) for the grid cell representing our study area, which exhibits a long-term increasing trend in both air temperature and precipitation. In the runoff simulation, this product was used with the bias corrected for solar radiation and wind velocity based on the difference between measured values during HY2011 and HY2012 and simulated values during HY2015 through HY2019. Table 3 summarizes the annual means or annual totals (for precipitation) of observed and simulated meteorological variables during a given period, with the bias corrected for solar radiation and wind velocity.

7 Model application and results

7.1 Runoff and water balance at present

Figure 6 shows a comparison of simulated flow rates with observed rates at HH1 from July 2011 to May 2013. In simulation 1, the observed vertical gradient of monthly precipitation and the daily lapse rate of air temperature were used. Seasonal variations in flow rates in the austral summer and winter were reproduced well for both HY2011 and HY2012. The three individual peaks simulated in the transition period of 2011 agree well with the observed data. These simulated peaks formed as a result of enhanced glacier melt due to higher air temperature and solar radiation on non-precipitation days. On the other hand, solar radiation and air temperature were lower between peaks, which reduced glacier melting. Some relevant peaks were not well reproduced by simulation 1, as indicated by the simulated peaks in January 2012, February 2012, and October 2012, which are smaller than those observed.

These discrepancies in flow rate can be attributed to several factors, such as spatially uneven snowfall and uncertainty regarding the air temperature at the ablation zone. The

HESSD
10, 13093–13144, 2013

air temperature profile across the ablation zone is likely an important factor inducing overestimated or underestimated glacier and snow melts. As mentioned before, higher discharge was observed in October 2012, but the simulated results did not show a large peak. This may be attributed to the prevailing wind from the south and southeast during this period, which means that the lapse rate may have been closer to that calculated for MT1–MH1 (Fig. 3). If this condition were considered in the model, the simulated discharge would be higher. For the lower flow rates in January 2012 and October 2012, we focused on the smaller vertical gradient in January 2012 compared with those in December 2011 and February 2012 (Fig. 4), which may be a result of uneven snowfall or some problem with the instrumentation.

Based on our insights into these causative factors, simulation 2 was run with the gradient of precipitation changed to the mean of December 2011 and February 2012 and the lapse rate set to 0.6 °C (100 m^{-1}) during October 2012. With these changes, the calculated flow rates were improved for these periods (Fig. 6), resulting in a coefficient of determination $R^2 = 0.91$, RMSE = 0.037 m^3 s^{-1}, and a Nash–Suttcliffe efficiency (Nash and Sutcliffe, 1970) NSE = 0.909. Additionally, the flow rate simulated without the retarding effect of the wetland and lake did not reproduce the observed variations well because it exhibited much greater fluctuation within a short period, thus resulting in $R^2 = 0.57$, RMSE = 0.099 m^3 s^{-1}, and NSE = 0.336. This implies that wetlands and lakes in the tropical Andes play significant roles in buffering runoff from glacier melt and supply this water gradually.

The mass balance of the glacier in our study area has not been measured, so it is difficult to compare our model with observations. Instead, the observed and calculated albedos at MHG were compared to ensure the accuracy of the equation used to calculate snow melt. Variations in the albedo measured at MHG and those simulated for the elevation zone of 5100–5200 m a.s.l. in simulation 2 are shown in Fig. 7. The variation in and magnitude of albedo at MHG are similar to those observed at Zongo Glacier at 5060 m a.s.l. (Sicart et al., 2011), although MHG is located at higher elevation (5150 m a.s.l.). As shown in Fig. 7, the temporal variation in the albedo agreed with

HESSD
10, 13093–13144, 2013

the observed, and the general characteristic of higher albedo after each snowfall event was reproduced. Periodic decreases in albedo during the dry season of 2012 do not relate strongly to the observed or simulated streamflow, whereas those in October and November 2012 correspond to an abrupt increase in observed streamflow (see Fig. 6). Although observational data for the first 6 months are missing, the simulated albedo for 2011 indicates that the condition of glacier melting, i.e. albedo equal to 0.25, was also met several times, which likely contributed to the temporal increase in streamflows observed during these periods (Fig. 6). These corresponding responses suggest that the glacier ice in the elevation zone between 5100 and 5200 m a.s.l. is exposed and melted because of high temperature and high shortwave radiation occurring during a short period of time due to weak and sporadic precipitation (Favier et al., 2004).

The sensitivity of the flow rate to air temperature distribution, or lapse rate, was examined because the air temperature distribution calculated by Eqs. (31) and (32) includes uncertainty arising from the interpolation method, especially when vapor and heat are advected by the strong valley wind to higher elevations over the glacierized areas and when the downward colder wind prevents glacier melting at lower elevation zones.

We compared flow rates simulated using a daily lapse rate 15 % smaller/larger than that calculated from the observed temperature gradients from MH1–MHG and MT1–MH1 using Eq. (28). The comparison revealed a large difference in flow rate between the two cases (±15 %) during the wet season, especially when runoff from the glacier and snow melt is dominant (Fig. 8). Most of the observed flow rates fall within the range calculated from the condition of current lapse rate ±15 %. The annual averages of the flow rate calculated with the higher lapse rate (+15 %) and the lower lapse rate (−15 %) were 15 % smaller and 18 % larger than that simulated using the original lapse rate condition, respectively. These results indicate that melting over the study area is more sensitive to an increase in air temperatures during the wet season, probably because the current temperature range in the area with greater glacial cover is relatively close to the freezing/melting point. Other factors that may contribute to uncertainty in

HESSD
10, 13093–13144, 2013

the simulated flow rates are the vertical gradient of precipitation and the precipitation phase because the vertical gradient of precipitation is different from event to event and place to place and because the phase cannot be separated by a single threshold air temperature.

The model calculates individual streamflow components from the different sources of runoff, i.e. glacier melt, snowmelt, and rainfall from glacierized areas and non-glacierized areas, via surface and subsurface flows, although observed components are not available for comparison. Figure 9 shows individual runoff components for each month during HY2011 and HY2012, which were simulated with a specifically adjusted lapse rate for air temperature and the vertical gradients of precipitation for January and October 2012, as introduced in simulation 2 (Fig. 6). It is noted that the runoff from each component is converted to water depth averaged over the whole catchment area to find the relative contribution to the total runoff depth. We can see that runoff from glacier melt is large in the transition period, especially during October and November in both years, and is reduced during the subsequent months of the wet season. Runoff from snowmelt in glacierized areas is comparable to or even larger than that from glacier melt during December to March, when glacier melt is prevented by snow cover on the glacier surface (Favier et al., 2004). In March and April 2013, glacier melt again becomes large because of the higher temperature and fewer precipitation events. Most of the glacier melt was calculated to occur in the elevation zones from 5000 m to 5200 m a.s.l., with an additional small runoff contribution from glacier melt below 5000 m a.s.l.

During the wet season, from December to February, runoff from snowmelt and subsurface flow in non-glacierized areas become much greater than the runoff from glacierized areas. This occurs because of the larger area of non-glacierized areas and quick snowmelt induced by the warmer surface of bedrock over the non-glacierized areas (Ribstein et al., 1995). Runoff from rainfall is currently limited, but this component may become significant in the future due to the long-term shift in precipitation phase from snow to rain caused by the temperature increase.

HESSD
10, 13093–13144, 2013

The 2 yr mean annual water balance in the Huayna Potosi West headwater catchment is summarized in Table 4. Precipitation (either by snow or rainfall) and reduced glacier volume are transferred to surface runoff, subsurface runoff, deep groundwater recharge, sublimation from the glacier surface and snow surface, evaporation from the ground, and storage as accumulated snow pack. The change in storage in the ground of non-glacierized areas is negligible. Runoff from glacier melt accounts for about 24.1 % of the annual total runoff (558.9 mm), and 65.4 % of the total runoff comes from surface and subsurface flow from the non-glacierized areas (365.3 mm), with subsurface runoff (204.8 mm) providing a larger contribution. Although these values are not verified by the observational data, a larger contribution from subsurface water is qualitatively consistent with hydrochemical analyses for streams in partially glacierized catchments of the Cordillera Blanca (Mark et al., 2005; Baraer et al., 2009).

7.2 Glacier retreat and runoff in the future (HY2011–2050)

Runoff and glacier retreat prediction was performed by applying the observed current meteorological conditions continuously until May 2051 with several cases of increasing air temperature trend ranging from 0 to 0.4 °C decade^{-1}. For this, a constant increment depending on the year since 2011 was added to the air temperature recorded during HY2011 and HY2012, and the other variables were kept the same as the current conditions. Monthly averaged lapse rates obtained from our 2 yr dataset were applied throughout the simulation periods. Additionally, adjusted MRI-AGCM outputs were applied until 2039.

Figure 10 shows the change in total glacierized area calculated with each case of future trends and MRI-AGCM output. In each case of future trends, the uncertainty related to the volume–area relationship was indicated by the upper and lower bounds of simulated glacierized areas. The upper bound indicates the result using the volume–area relationship by Baraer et al. (2012) (case A), and the lower bound is the result calculated by considering two main separated glaciers as individual isolated glaciers while the initial total glacierized area is the same as case A (case B). The setting of

HESSD
10, 13093–13144, 2013

the glacier volume–area relationship affects the change in total glacierized area, but the difference between case A and case B is not so significant. Each result of the reduction in glacierized area is within a small range of difference by around HY2020, after which the difference between each case of future trends gradually becomes wider until HY2050.

In case A, if the current meteorological conditions persist until HY2050 with the air temperature kept as its current level (0.0 °C decade^{-1}), the glacier will be reduced by about 31.7 % in 2050 due to melting of glacier located below 5200 m a.s.l. If we assume the air temperature increase of 0.2 °C decade^{-1}, which is within the range of possible increases in the tropical Andes, the reduction is more rapid and serious, resulting in a 64.4 % area decrease by HY2050 in case A compared with HY2011. The change in glacierized area obtained by applying MRI-AGCM output is close to the results of the temperature trends of 0.2 °C decade^{-1} and 0.3 °C decade^{-1} even though the air temperature trend of MRI-AGCM was higher (0.4 °C decade^{-1}). This is due to the effect of the increasing trend of annual precipitation predicted by MRI-AGCM (6.4 mm yr^{-1}), which tends to reduce the period during which the glacier is exposed.

The cumulative mass balance shown in Fig. 11 was calculated as the total of water volume change by snow accumulation in higher elevation zones and glacier ablation in lower elevation zones, with the glacierized area at each time step as a reference. The lower bound of each case indicates the result from the volume–area relationship by Baraer et al. (2012) (case A), and the upper bound is calculated by considering the effect of separated glaciers on the estimated total glacier volume (case B). The uncertainty range of cumulative mass balance increases as time passes, especially for cases with a higher temperature trend. When the trend is 0.1 °C decade^{-1}, cumulative mass balance to the end of HY2050 reaches about 22.5 m w.e. (0.56 m w.e. yr^{-1}) in case A, which is similar to that reported for Zongo Glacier (Soruco et al., 2009b). When the trend is doubled (0.2 °C decade^{-1}), the cumulative mass balance is also almost doubled (0.99 m w.e. yr^{-1}) from the case of 0.1 °C decade^{-1} in case A and is closer to the observed mass balance of tropical glaciers in the Andes with a maximum altitude

HESSD
10, 13093–13144, 2013

lower than 5400 m a.s.l., including Charquini Sur in Bolivia (Rabatel et al., 2013). MRI-AGCM outputs give a mass balance (1.40 m w.e. yr^{-1}) similar to that for 0.3 °C $decade^{-1}$ in case A owing to the effect of reduced period in glacier exposure. If we assume no trend of air temperature, cumulative mass balance is close to zero, and the range of uncertainty is the minimum.

The different trends in the reduction depend on two processes related to air temperature. Naturally, the temperature increase will enhance snow and glacier melt, resulting in a decrease in glacier volume and area and an increase in non-glacierized areas. Additionally, when air temperature increases, the chance of snow decreases, and more rainfall may occur. Then, glacier melt will be enhanced as the time during which the glacier is exposed becomes longer, which accelerates glacier retreat. Consequently, runoff components and the resulting hydrographs are expected to shift from the current condition with large contributions from glacier and snow melt in glacierized areas (Fig. 9) to those more influenced by runoff from rainfall and subsurface flow from non-glacierized areas (Fig. 12). Comparing Fig. 12a and b, it is clear that the larger the increasing trend of air temperature is, the greater the surface runoff from rainfall in the non-glacierized area becomes. In the transition period, snowmelt from the glacierized area becomes greater due to the rising temperature trend, while total runoff is reduced from that at present (Fig. 9). As a result, seasonal variation becomes greater, which means that more streamflow occurs in the wetter season and less in the drier season.

Long-term changes in runoff components are shown in Fig. 13 for three cases of temperature trend, i.e. 0.0 °C $decade^{-1}$, 0.1 °C $decade^{-1}$, and 0.2 °C $decade^{-1}$ with a volume–area relationship given by case A, and the case of MRI-AGCM output. The figure indicates that the contribution of runoff from glacier and snow melts in the glacierized areas tends to decrease toward 2050 (Fig. 13a–c) because the glacier is not in equilibrium, and the size of glacier decreases as a result of its retreat. Conversely, in cases (b) and (c), runoff from non-glacierized areas increases because of area enlargement, increased surface runoff from rainfalls, and more subsurface flow because of increased infiltration and storage in non-glacierized areas (Fig. 13b and c). On the other hand, if

HESSD
10, 13093–13144, 2013

the air temperature does not increase into the future (Fig. 13a), total runoff decreases due to reduced runoff from glacier and snow melts, and the cumulative mass balance is very small compared with the larger negative mass balances of the cases shown in Fig. 13b–d (Fig. 11). Therefore, in this case, accumulated snow makes up a long-term water storage that, along with the glacier, will contribute to runoff when it is exposed under higher temperature conditions.

Figure 13 indicates that the annual total runoff for cases (b) and (c) increases once toward the early 2020s but that it then decreases, resulting in a slight overall change from 559 mm during HY2011 and HY2012 to 542 mm and 572 mm during HY2049 and HY2050, respectively. The nature of the slight change is mainly because of increased subsurface runoff and rainfall runoff. However, the change in seasonal variation is more critical when we need to adapt to the reduced glacier effect. Our model predicts that by HY2050, seasonal variation becomes large because glacial meltwater decreases and rain-fed runoff becomes large, leading to limited available water resources during the dry season, although a small amount of flow may be maintained in the dry season by subsurface runoff (Fig. 12). The combined impact of air temperature increase and precipitation increase shown in Fig. 13d indicates that although the annual runoff shows large variations, its trend is not clear, whereas seasonal variation is increased as in the other cases.

7.3 Influence of other factors

Future glacier and snow melts and their accompanying runoff depend not only on the trends of air temperature and precipitation but also on other variables, such as humidity, solar radiation, wind velocity, and the condition of surface cover, all of which interactively define the local meteorological conditions.

The trend of relative humidity derived from historical records is not significant (Vuille et al., 2008); thus, if this trend continues into the future, the effect on melting and runoff would be minimal. We confirmed this by model simulation using an increasing trend of 1 % decade^{-1} for the annual mean relative humidity. Solar radiation is affected by

HESSD
10, 13093–13144, 2013

cloud cover and precipitation, and these factors are highly variable in time and space. If precipitation increases in the future, solar radiation may be reduced, and processes related to solar radiation such as glacier and snow melt will also be affected. In this study, these interactive situations were considered to some extent by introducing GCM outputs, but a more robust approach by resolving the catchment with finer future climate conditions calibrated by observed meteorological variables is necessary. In this perspective, our monitoring data, together with data from other AWSs in the same region, will contribute to the application of hydrological models to other watersheds, especially the larger ones, which will provide more comprehensive information about how to adapt to the change in available water resources in an environment of less glacial meltwater.

In addition to the meteorological environment, watersheds may also experience changes in surface conditions, such as land cover, soils, and topography. In warmer environments, the land surface may change from bare soil to vegetated cover, which would result in water storage but also increased evapotranspiration. Furthermore, runoff control by water storage and the retarding effect of permanent wetlands and lakes would also be expected, although a detailed analysis of their hydrological effects has not been performed. Therefore, long-term monitoring to detect the hydrological impact of wetlands and vegetative cover, focusing especially on the dry season, will be particularly important for water resources assessment in the Andes in a changing climate.

8 Conclusions

We developed a semi-distributed conceptual model to simulate runoff in a partially glacierized catchment in the tropical Andes under changing climate. The model calculates daily runoff from subdivided elevation zones considering inherent topographic conditions, spatial and temporal variability in meteorological conditions, hydrological effects of wetlands and lakes, and change in long-term glacier cover.

HESSD
10, 13093–13144, 2013

We applied the model to the Huayna Potosi West headwater catchment in the Cordillera Real, Bolivia, to evaluate its ability to reproduce current seasonal streamflow variations and quantify the glacio-hydrological response of the catchment during 2 yr from June 2011 until May 2013. The characteristic seasonal and temporal variations in daily streamflow were simulated well by the model, largely because of the inclusion of characteristic geographic, climatic, and hydrological conditions of the catchment. We indicated that the vertical gradient of air temperature strongly influenced the runoff magnitude due to enhanced glacier and snow melt over the glacierized area. We quantified components from different sources of runoff and suggested that the current runoff is sustained mainly by glacier melt in the early stage of the wet season, October and November, and by contributions from snowmelt and subsurface runoff from the non-glacierized areas during the subsequent months in the wet season.

Long-term changes in runoff, glacierized area, and cumulative glacier and snow mass balance were quantified using several cases of future trends of air temperature and precipitation that were based on observed and predicted results. We found that the annual runoff is not changed very much by different temperature trends in the three cases, but seasonal variation is modified significantly, as seen in reduced streamflow in the dry season and early wet season and increased streamflow in the wet season, especially in January and February. The runoff components calculated with the possible trend of air temperature increase ($0.2\,^{\circ}\mathrm{C\,decade^{-1}}$) suggest that by 2050, subsurface flow becomes more dominant and that direct runoff from rainfall becomes comparable to that from snowmelt due to elevated air temperature and elevated altitude of the snow line. The model predicts that the change in glacier cover continues until 2050 even if there is no long-term temperature increase and that wider variations in cumulative mass balance are expected to occur depending on the trend of increasing air temperature.

To assess the future water resources available from Tuni Lake, we need to apply the model to other areas including the Condoriri Glacier catchment located in the same mother catchment. To apply it to larger catchments, we may need to improve

HESSD
10, 13093–13144, 2013

the model by including the flow routing process and considering the different hydrological response of individual land-cover types, such as bedrock, grassland, and wetlands. In this paper, the future scenarios were relatively simple and were also limited to the application of a single GCM output. For better decision making, however, it is important to provide streamflow variations predicted by using a larger number of possible future climate projections and to validate these with continuous and long-term monitoring of streamflow and meteorological variables.

Acknowledgements. This research was conducted under the Glacier Retreat Impact Assessment and National Policy Development (GRANDE) project supported by the Science and Technology Research Partnership for Sustainable Development (SATREPS), which was funded by the Japan Science and Technology Agency (JST) and the Japan International Cooperation Agency (JICA). We especially thank Ms. Y. Okamura and Mr. F. Rojas for their support in obtaining data of AWSs. MRI-AGCM outputs were produced under the "Projection of the Change in Future Weather Extremes Using Super High-Resolution Atmospheric Models" project supported by the KAKUSHIN Program of the Ministry of Education, Culture, Sports, Science and Technology (MEXT), Japan.

References

Baraer, M., McKenzie, J. M., Mark, B. G., Bury, J., and Knox, S.: Characterizing contributions of glacier melt and groundwater during the dry season in a poorly gauged catchment of the Cordillera Blanca (Peru), Adv. Geosci., 22, 41–49, doi:10.5194/adgeo-22-41-2009, 2009.

Baraer, M., Mark, B. G., McKenzie, J. M., Condom, T., Bury, J., Huh, K.- I., Portocarrero, C., Gomez, J., and Rathay, S.: Glacier recession and water resources in Peru's Cordillera Blanca, J. Glaciol., 58, 134–150, 2012.

Bradley, R. S., Vuille, M., Diaz, H. F., and Vergara, W.: Threats to water supplies in the tropical Andes, Science, 312, 1755–1756, 2006.

Caballero, Y., Chevalier, P., Gallaire, R., and Pillco, R.: Flow modeling in a high mountain valley equipped with hydropower plants: Rio Zongo Valley, Cordillera Real, Bolivia, Hydrol. Process., 18, 939–957, 2004.

HESSD

10, 13093–13144, 2013

Favier, V., Wagnon, P., and Ribstein, P.: Glaciers of the outer and inner tropics: a different behaviour but a common response to climatic forcing, Geophys. Res. Lett., 31, L16403, doi:10.1029/2004GL020654, 2004.

Francou, B., Ribstein, P., Saravia, R., and Tiriau, E.: Monthly balance and water discharge of an intertropical glacier: Zongo Glacier, Cordillera Real, Bolivia, 16° S, J. Glaciol., 41, 61–67, 1995.

Francou, B., Vuille, M., Wagnon, P., Mendoza, J., and Sicart, J. E.: Tropical climate change recorded by a glacier in the central Andes during the last decades of the twentieth century: Chacaltaya, Bolivia, 16° S, J. Geophys. Res., 108, 4154, doi:10.1029/2002JD002959, 2003.

Fu, P. and Rich, P.: Solar Analyst 1.0 User Manual, Helios Environmental Modeling Institute, 2000.

Hock, R.: A distributed temperature-index ice- and snowmelt model including potential direct solar radiation, J. Glaciol., 45, 101–111, 1999.

Hock, R.: Temperature index melt modelling in mountain areas, J. Hydrol., 282, 104–115, 2003.

Huss, M., Farinotti, D., Bauder, A., and Funk, M.: Modelling runoff from highly glacierized alpine drainage basins in a changing climate, Hydrol. Process., 22, 3888–3902, 2008.

IPCC: Climate Change 2007: Impacts, Adaptation and Vulnerability Contributions of Working Group II to the Forth Assessment Report of the Intergovernmental Panel on Climate Change, WMO/UNEP, Cambridge University Press, Cambridge, 2007.

Juen, I., Kaser, G., and Georges, C.: Modelling observed and future runoff from a glacierized tropical catchment (Cordillera Blanca, Perú), Global Planet. Change, 59, 37–48, 2007.

Kaser, G.: A review of the modern fluctuations of tropical glaciers, Global Planet. Change, 22, 93–103, 1999.

Kitoh, A., Kusunoki, S., and Nakaegawa, T.: Climate change projections over South America in the late 21st century with the 20 and 60 km mesh Meteorological Research Institute atmospheric general circulation model (MRI-AGCM), J. Geophys. Res., 116, D06105, doi:10.1029/2010JD014920, 2011.

Konz, M., Uhlenbrook, S., Braun, L., Shrestha, A., and Demuth, S.: Implementation of a process-based catchment model in a poorly gauged, highly glacierized Himalayan headwater, Hydrol. Earth Syst. Sci., 11, 1323–1339, doi:10.5194/hess-11-1323-2007, 2007.

Liu, T., Kinouchi, T., and Ledezma, F.: Characterization of recent glacier decline in the Cordillera Real by LANDSAT, ALOS, and ASTER data, Remote Sens. Environ., 137, 158–172, 2013.

HESSD
10, 13093–13144, 2013

Mark, B. G. and Seltzer, G. O.: Recent glacial recession in the Cordillera Blanca, Peru (AD 1962–1999), Quaternary Sci. Rev., 24, 2265–2280, 2005.
Mark, B. G., McKenzie, J. M., and Gomez, J.: Hydrochemical evaluation of changing glacier meltwater contribution to stream discharge: Callejon de Huaylas, Peru, Hydrol. Sci. J., 50, 975–987, 2005.
Martinec, J., Rango, A., and Roberts, R.: Snowmelt Runoff Model (SRM) user's manual, updated edition for Windows, Spec. Rep. 100, N. M. State Univ., Las Cruces, N. M., 2008.
Moore, R. D.: Application of a conceptual streamflow model in a glacierized drainage basin, J. Hydrol., 150, 151–168, 1993.
Moya Quiroga, V., Mano, A., Asaoka, Y., Kure, S., Udo, K., and Mendoza, J.: Snow glacier melt estimation in tropical Andean glaciers using artificial neural networks, Hydrol. Earth Syst. Sci., 17, 1265–1280, doi:10.5194/hess-17-1265-2013, 2013.
Nash, J. E. and Sutcliffe, J. V.: River flow forecasting through conceptual models, Part I: A discussion of principles, J. Hyrol., 10, 282–290, 1970.
Naz, B. S., Frans, C. D., Clarke, G. K. C., Burns, P., and Lettenmaier, D. P.: Modeling the effect of glacier recession on streamflow response using a coupled glacio-hydrological model, Hydrol. Earth Syst. Sci. Discuss., 10, 5013–5056, doi:10.5194/hessd-10-5013-2013, 2013.
Nolin, A. W., Phillippe, J., Jefferson, A., and Lewis, S. L.: Present-day and future contributions of glacier runoff to summertime flows in a Pacific Northwest watershed: implications for water resources, Water Resour. Res., 46, W12509, doi:10.1029/2009WR008968, 2010.
Ohno, H., Ohata, T., and Higuchi, K.: The influence of humidity on the ablation of continental-type glaciers, Ann. Glaciol., 16, 107–113, 1992.
Pellicciotti, F., Brock, B., Strasser, U., Burlando, P., Funk, M., and Corripio, J.: An enhanced temperature-index glacier melt model including the shortwave radiation balance: development and testing for Haut Glacier d'Arolla, Switzerland, J. Glaciol., 51, 573–587, 2005.
Pepin, N. C. and Lundquist, J. D.: Temperature trends at high elevations: patterns across the globe, Geophys. Res. Lett., 35, L14701, doi:10.1029/2008GL034026, 2008.
Pouyaud, B., Zapata, M., Yerren, J., Gomez, J., Rosas, G., Suarez, W., and Ribstein, P.: On the future of the water resources from glacier melting in the Cordillera Blanca, Peru, Hydrol. Sci. J., 50, 999–1022, 2005.
Rabatel, A., Francou, B., Soruco, A., Gomez, J., Cáceres, B., Ceballos, J. L., Basantes, R., Vuille, M., Sicart, J.-E., Huggel, C., Scheel, M., Lejeune, Y., Arnaud, Y., Collet, M., Condom, T., Consoli, G., Favier, V., Jomelli, V., Galarraga, R., Ginot, P., Maisincho, L., Men-

HESSD
10, 13093–13144, 2013

doza, J., Ménégoz, M., Ramirez, E., Ribstein, P., Suarez, W., Villacis, M., and Wagnon, P.: Current state of glaciers in the tropical Andes: a multi-century perspective on glacier evolution and climate change, The Cryosphere, 7, 81–102, doi:10.5194/tc-7-81-2013, 2013.

Ramirez, E. and Francou, B.: Small glaciers disappearing in the tropical Andes: a case-study in Bolivia: Glaciar Chacaltaya (16° S), J. Glaciol., 47, 187–194, 2001.

Ribstein, P., Tiriau, E., Francou, B., and Saravia, R.: Tropical climate and glacier hydrology: a case study in Bolivia, J. Hydrol., 165, 221–234, 1995.

Schaefli, B., Hingray, B., Niggli, M., and Musy, A.: A conceptual glacio-hydrological model for high mountainous catchments, Hydrol. Earth Syst. Sci., 9, 95–109, doi:10.5194/hess-9-95-2005, 2005.

Schaper, J., Martinec, J., and Seidel, K.: Distributed mapping of snow and glaciers for improved runoff modelling, Hydrol. Process., 13, 2023–2031, 1999.

Sicart, J. E., Hock, R., Ribstein, P., Litt, M., and Ramirez, E.: Analysis of seasonal variations in mass balance and meltwater discharge of the tropical Zongo Glacier by application of a distributed energy balance model, J. Geophys. Res., 116, D13105, doi:10.1029/2010JD015105, 2011.

Soruco, A., Vincent, C., Francou, B., and Gonzalez, J. F.: Glacier decline between 1963 and 2006 in the Cordillera Real, Bolivia, Geophys. Res. Lett., 36, L03502, doi:10.1029/2008GL036238, 2009a.

Soruco, A., Vincent, C., Francou, B., Ribstein, P., Berger, T., Sicart, J. E., Wagnon, P., Arnaud, Y., Favier, V., and Lejeune, Y.: Mass balance of Glaciar Zongo, Bolivia, between 1956 and 2006, using glaciological, hydrological and geodetic methods, Ann. Glaciol., 50, 1–8, 2009b.

Stahl, K., Moore, R. D., Shea, J. M., Hutchinson, D., and Cannon, A. J.: Coupled modelling of glacier and streamflow response to future climate scenarios, Water Resour. Res., 44, W02422, doi:10.1029/2007WR005956, 2008.

Urrutia, R. and Vuille, M.: Climate change projections for the tropical Andes using a regional climate model: temperature and precipitation simulations for the end of the 21st century, J. Geophys. Res., 114, D02108, doi:10.1029/2008JD011021, 2009.

Vera, C., Silvestri, G., Liebmann, B., and Gonzalez, P.: Climate change scenarios for seasonal precipitation in South America from IPCC-AR4 models, Geophys. Res. Lett., 33, L13707, doi:10.1029/2006GL025759, 2006.

HESSD
10, 13093–13144, 2013

Vergara, W., Deeb, A. M., Valencia, A. M., Bradley, R. S., Francou, B., Zarzar, A., Grünwaldt, A., and Haeussling, S. M.: Economic impacts of rapid glacier retreat in the Andes, Eos Trans. AGU, 88, 261–264, doi:10.1029/2007EO250001, 2007.

Vuille, M. and Bradley, R. S.: Mean annual temperature trends and their vertical structure in the tropical Andes, Geophys. Res. Lett., 27, 3885–3888, 2000.

Vuille, M., Bradley, R. S., Werner, M., and Keimig, F.: 20th century climate change in the tropical Andes: observations and model results, Climatic Change, 59, 75–99, 2003.

Vuille, M., Francou, B., Wagnon, P., Juen, I., Kaser, G., Mark, B. G., and Bradley, R. S.: Climate change and tropical Andean glaciers – past, present and future, Earth Sci. Rev., 89, 79–96, doi:10.1016/j.earscirev.2008.04.002, 2008.

Wagnon, P., Ribstein, P., Schuler, T., and Francou, B.: Flow separation on Zongo Glacier, Cordillera Real, Bolivia, Hydrol. Process., 12, 1911–1926, 1998.

Wanchang, Z., Yinsheng, Z., Ogawa, K., and Yamaguchi, Y.: Observation and estimation of daily actual evapotranspiration and evaporation on a glacierized watershed at the headwater of the Urumqi River, Tianshan, China, Hydrol. Process., 13, 1589–1601, 1999.

HESSD
10, 13093–13144, 2013

Table 1. Melting factors for snow and glacier.

Type of melting	a_{1g}, a_{1gs}, a_{1s}	a_{2g}, a_{2gs}, a_{2s}
Glacier melt M_g	4.5 ($mm\,d^{-1}\,°C^{-1}$)	0.07 ($m^2\,mm\,W^{-1}\,day^{-1}\,°C^{-1}$)
Snowmelt on the glacier M_{gs}	2.1 ($mm\,d^{-1}\,°C^{-1}$)	0.03 ($m^2\,mm\,W^{-1}\,day^{-1}\,°C^{-1}$)
Snowmelt on the ground M_{ngs}	8.0 ($mm\,d^{-1}\,°C^{-1}$)	0.26 ($m^2\,mm\,W^{-1}\,day^{-1}$)

HESSD
10, 13093–13144, 2013

Table 2. List of parameters used in the model.

Category	Parameter
Snow and glacier albedo	$s^* = 6$ (mm), $n^* = 3$ (days) $\alpha_{firn} = 0.5$, $\alpha_{gnd} = 0.20$, $\alpha_{ice} = 0.25$, $\alpha_{fresh} = 0.88$ ($T_a =< -4.6$) $= 0.88 - 0.015(T_a + 4.6)(T_a > -4.6)$
Runoff coefficient	$c_{ngs,min} = 0.1$, $c_{ngs,max} = 0.5$, $c_{gm} = 1.0$, $c_{gs} = 1.0$, $c_{gr} = 1.0$, c_{ngs}, c_{ngr}: Eq. (36)
Subsurface flow coefficient	$k_{ng} = 0.03$
Ground conditions	$S_{max} = 200$ (mm), Inf = 1000 (mm d^{-1}), $\alpha_{gnd} = 0.2$
Topographic shading factor	$SR_i = 0.286 \sim 1.252$ (monthly values are given)

HESSD
10, 13093–13144, 2013

Table 3. Comparison of observed meteorological conditions with MRI-AGCM outputs.

Annual mean or total	Observed at MH1 (Jun 2011–May 2013)	MRI-AGCM (Jun 2015–May 2020)	MRI-AGCM (Jun 2015–May 2039)
Air temperature (°C)	2.86	3.08	3.38
Relative humidity (%)	61.3	64.3	65.9
Wind velocity ($m s^{-1}$)	2.15	2.15	2.13
Solar radiation ($W m^{-2}$)	208.1	208.1	205.1
Precipitation ($mm yr^{-1}$)	566.7	498.7	564.9

HESSD
10, 13093–13144, 2013

Table 4. Mean annual water balance and contribution from glacierized and non-glacierized areas.

Component	Glacierized area (mm)	Non-glacierized area (mm)	Total (mm)
Precipitation	178.1	693.3	871.4
Glacier mass reduction	155.1	–	155.1
Runoff (total)	193.6	365.3	558.9
Runoff from glacier melt	134.3	–	134.3
Runoff from snowmelt	55.8	133.5	189.3
Runoff from rainfall	3.6	27.0	30.5
Subsurface flow runoff	–	204.8	204.8
Deep groundwater	–	176.8	176.8
Sublimation and evaporation	70.8	151.2	222.0
Snow accumulation	68.9	0.0	68.9

HESSD
10, 13093–13144, 2013

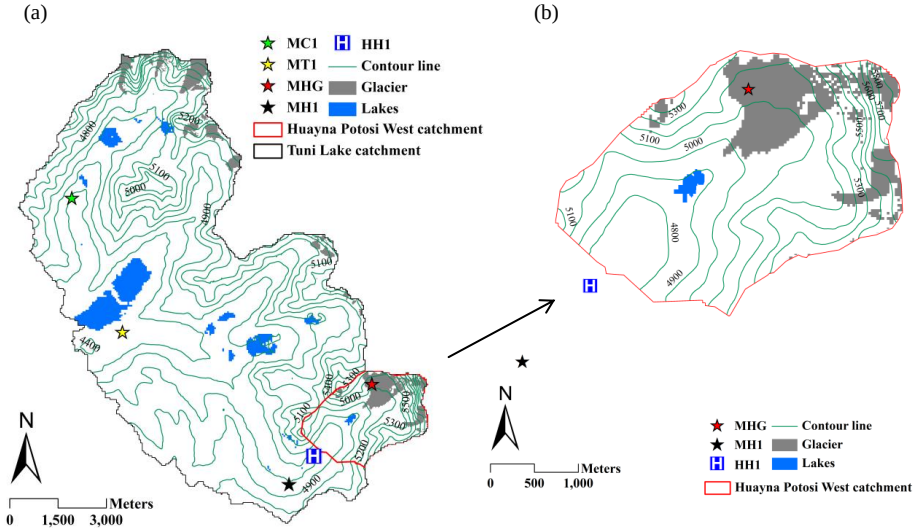

Fig. 1. Study area showing **(a)** Tuni Lake catchment and **(b)** Huayna Potosi West headwater catchment. HH1 is a hydrological station located at the outlet of Huayna Potosi West headwater catchment. MC1, MT1, MHG, and MH1 are automated weather stations.

HESSD
10, 13093–13144, 2013

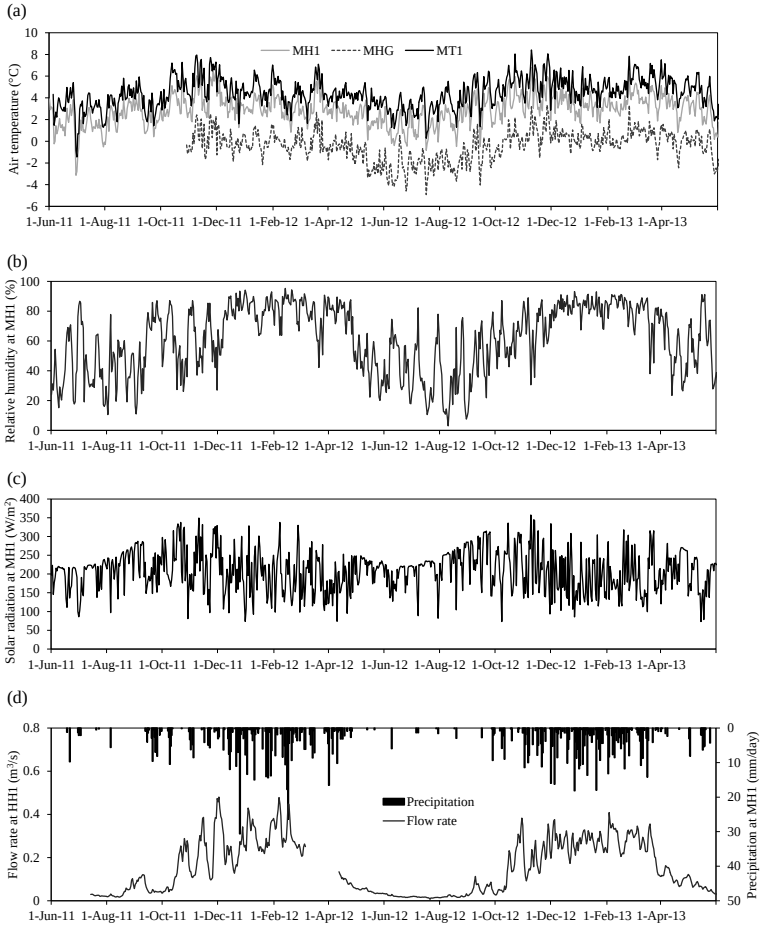

Fig. 2. Observed daily mean **(a)** air temperatures, **(b)** relative humidity, **(c)** solar radiation, and **(d)** daily total precipitation and daily mean flow rate.

HESSD
10, 13093–13144, 2013

Modeling glacier melt and runoff in a high-altitude headwater catchment

T. Kinouchi et al.

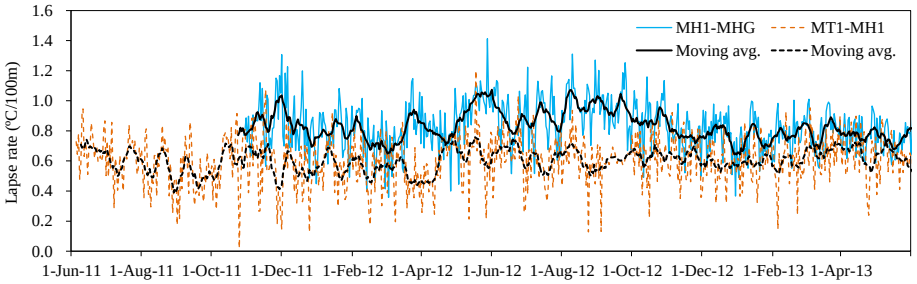

Fig. 3. Daily and moving-average (10 day) lapse rate of air temperature.

HESSD
10, 13093–13144, 2013

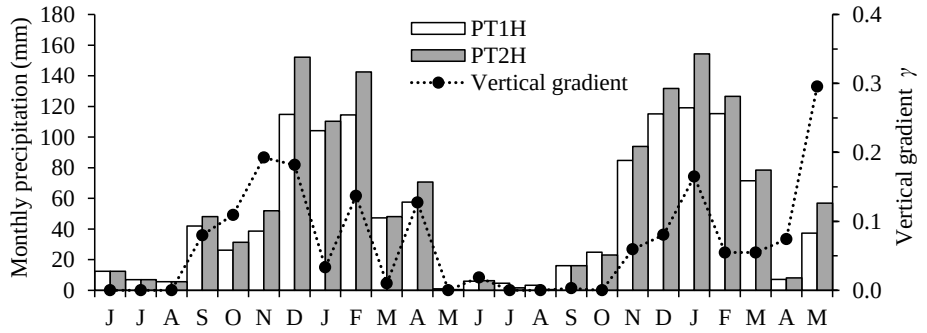

Fig. 4. Monthly precipitation and its vertical gradient during HY2011 and HY2012. Gradient γ is used in Eq. (30) and is defined as the vertical gradient of precipitation per 100 m elevation difference given by observed monthly precipitation at PT1H and PT2H.

HESSD
10, 13093–13144, 2013

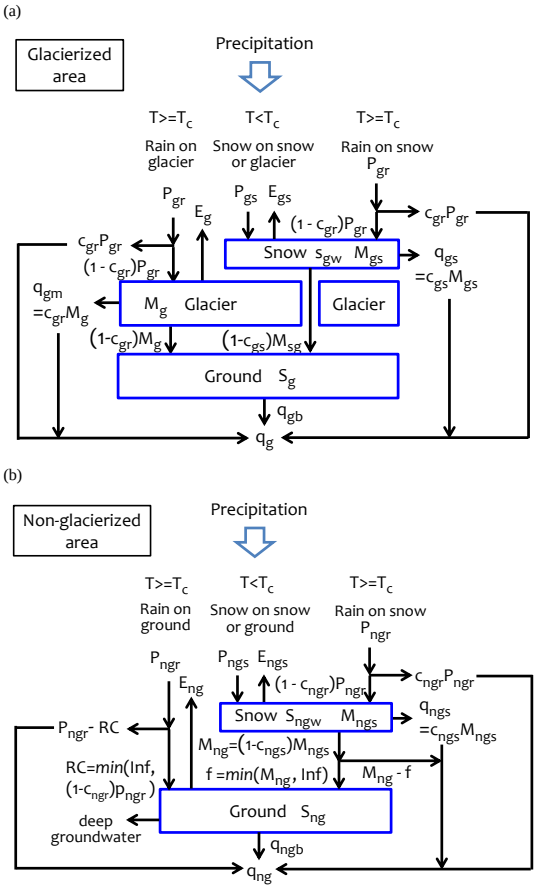

Fig. 5. Structure of runoff calculation in the model for **(a)** glacierized and **(b)** non-glacierized areas. In some symbols, the subscript *i* for elevation zone is omitted.

HESSD
10, 13093–13144, 2013

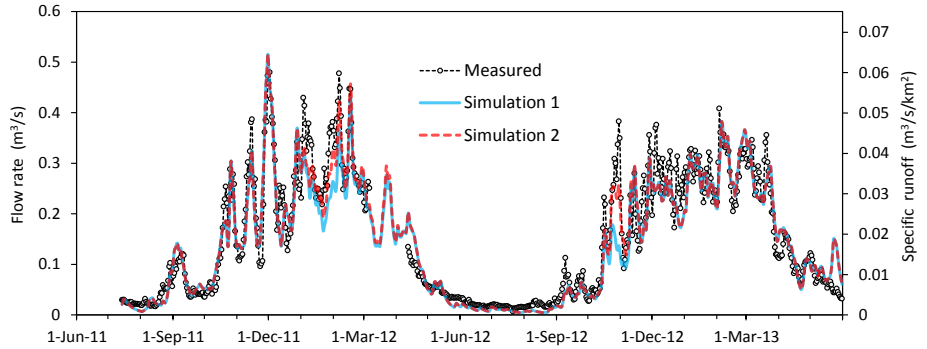

Fig. 6. Comparison between simulated flow rates and those measured at HH1. In simulation 1, the observed vertical gradient of monthly precipitation and the daily lapse rate of air temperature are used. In simulation 2, the gradient of precipitation was changed to the mean of December 2011 and February 2012, and the lapse rate was set to 0.6 °C (100 m^{-1}) during October 2012. The vertical axis on the right-hand side indicates the specific runoff.

HESSD
10, 13093–13144, 2013

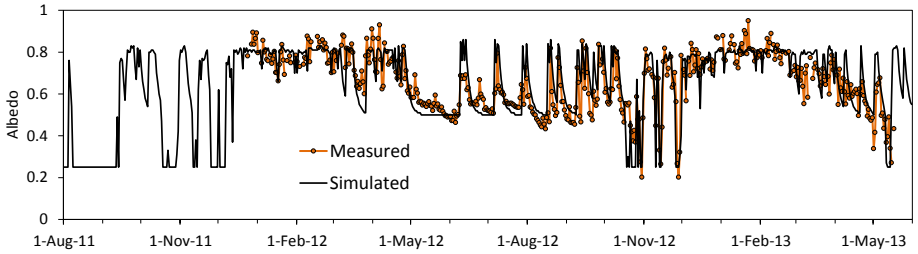

Fig. 7. Comparison of albedo measured at MHG and simulated for elevation band 5100–5200 m a.s.l.

HESSD
10, 13093–13144, 2013

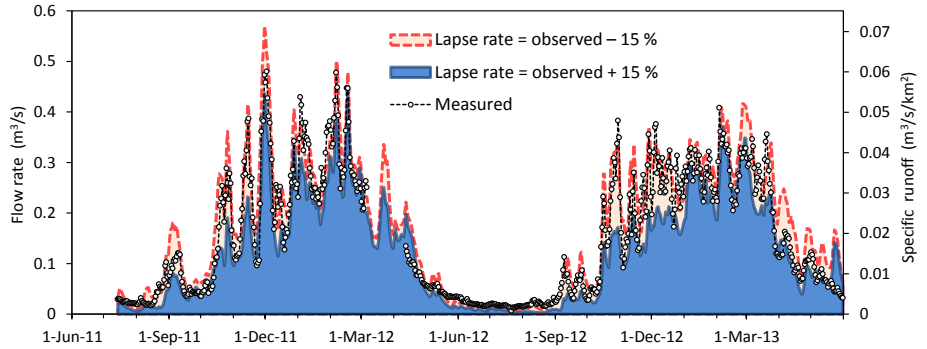

Fig. 8. Sensitivity of calculated flow rates to air temperature conditions. The vertical axis on the right-hand side indicates the specific runoff.

HESSD
10, 13093–13144, 2013

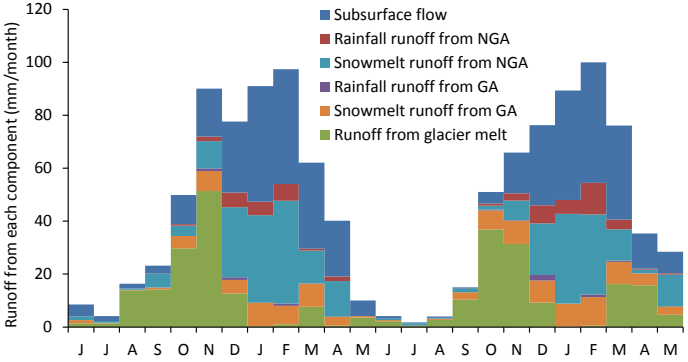

Fig. 9. Simulated monthly runoff components from June 2011 to May 2013.

HESSD
10, 13093–13144, 2013

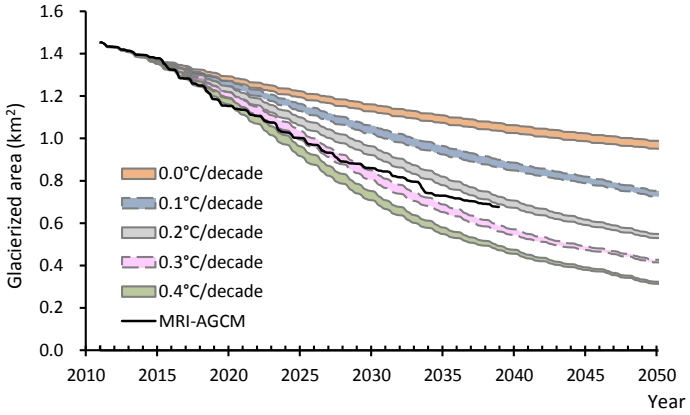

Fig. 10. Change in total glacierized area in the study catchment. The upper bound of each case indicates the result from the original volume–area relationship by Baraer et al. (2012) (case A). The lower bound is calculated by considering the effect of separated glaciers on the estimated total glacier volume (case B). The solid line of MRI-AGCM is the result for case A.

HESSD
10, 13093–13144, 2013

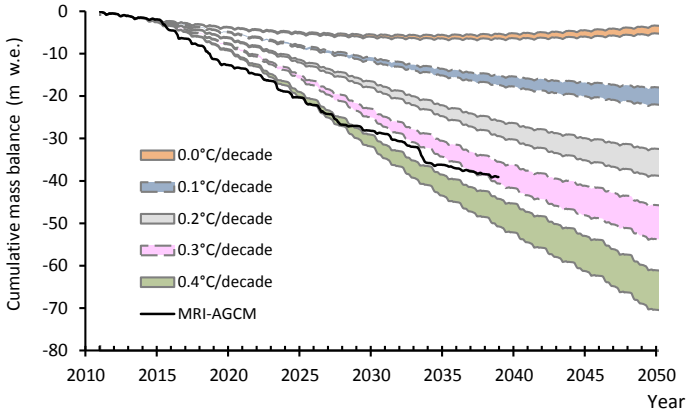

Fig. 11. Cumulative snow and glacier mass balance in the study catchment. The lower bound of each case indicates the result using the volume–area relationship by Baraer et al. (2012) (case A). The upper bound is calculated by considering the effect of separated glaciers on the estimated total glacier volume (case B). The solid line of MRI-AGCM is the result for case A.

HESSD
10, 13093–13144, 2013

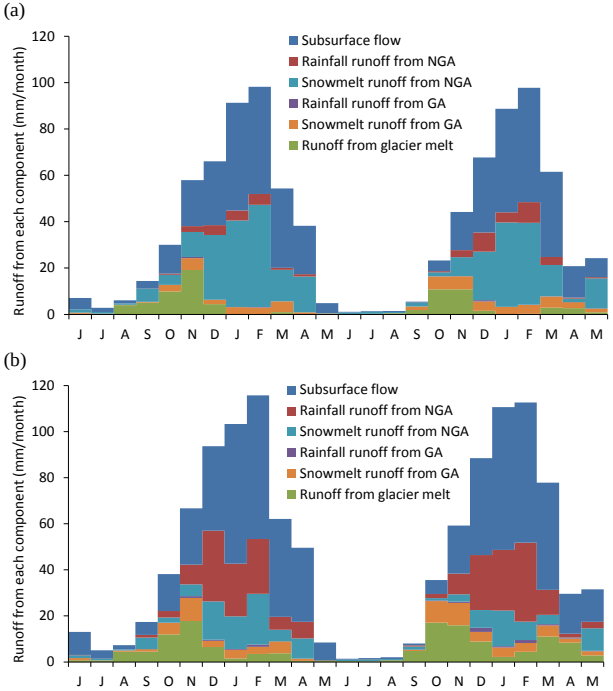

Fig. 12. Runoff components for the period HY2049 and HY2050 calculated with **(a)** no temperature trend and **(b)** temperature increase trend of 0.2 °C decade^{-1}. The volume–area relationship in case A is used.

HESSD
10, 13093–13144, 2013

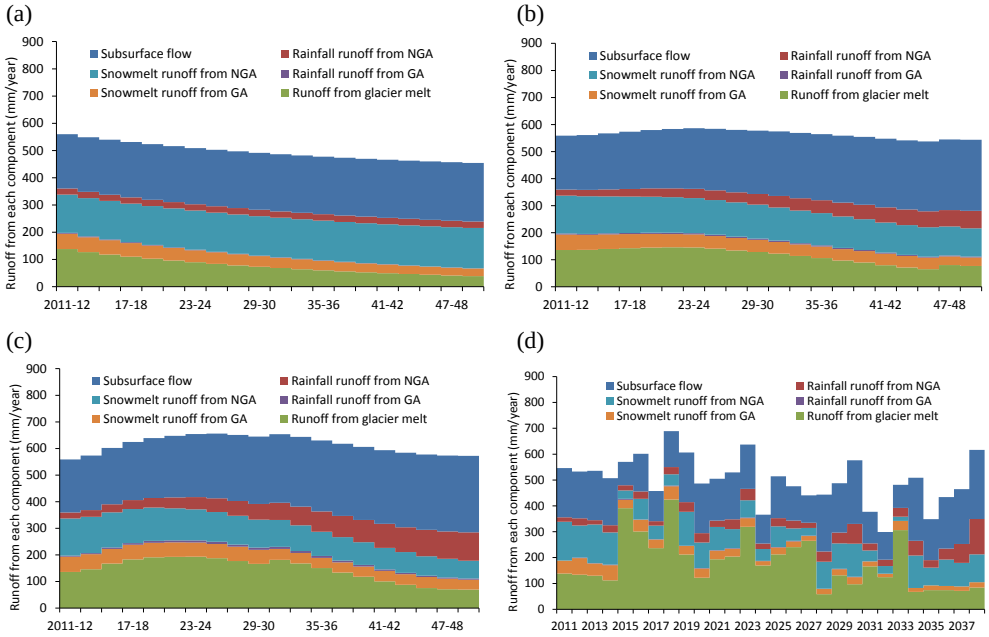

Fig. 13. Long-term change in runoff components calculated with **(a)** no temperature trend, **(b)** temperature increase trend of 0.1 °C decade^{-1}, **(c)** temperature increase trend of 0.2 °C decade^{-1}, and **(d)** MRI-AGCM outputs used as forcing data. The volume–area relationship in case A is used. Two-year average values are plotted from HY2011 to HY2050 in **(a)** to **(c)** and annual values are plotted from HY2011 to HY2038 in **(d)**.

HESSD
10, 13093–13144, 2013